Supplemental Material for Quasiballistic Thermal Transport from Nanoscale Heaters and the Role of the Spatial Frequency

Xiangwen Chen,[1,†] Chengyun Hua,[2,†] Hang Zhang,[3] Navaneetha K. Ravichandran,[4] Austin J. Minnich[1,*]

[1]*Division of Engineering and Applied Science, California Institute of Technology, Pasadena, CA 91125, USA*
[2]*Oak Ridge National Laboratory, Oak Ridge, TN 37831, USA*
[3]*Institute of Engineering Thermophysics, Chinese Academy of Sciences, Beijing 100190, China*
[4]*Department of Physics, Boston College, Chestnut Hill, MA 02467, USA*

(Dated: November 8, 2018)

[†]These authors contributed equally to this work.
[*]E-mail: aminnich@caltech.edu

1. Fitting of experimental and synthetic TDTR data

In this section we plot an example of the experimental and synthetic TDTR data along with fitting using the traditional model and our four-parameter model. Figure S1a shows the inadequacy of the traditional model to explain the experiments at room temperature for the line array. Figure S1b shows the deviation in fitting is qualitatively reproduced in the synthetic data computed using the BTE for the same structure used in the experiments. Both the experimental data and synthetic data can be fit by the four-parameter model as shown in Figs. S1c and d, respectively.

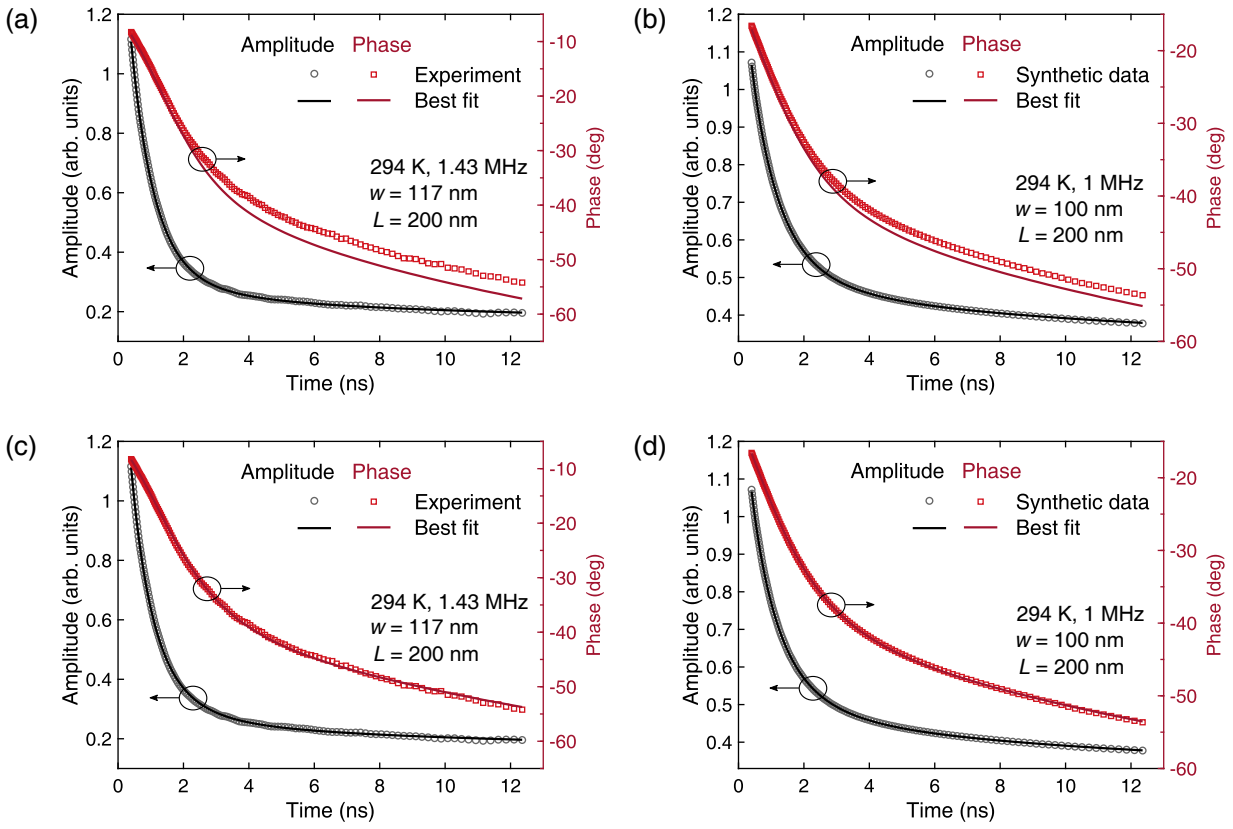

FIG. S1: Example fitting of experimental and synthetic TDTR data. Representative TDTR amplitude and phase experimental data (a) at 1.43 MHz with traditional Fourier model for w = 117 nm and L = 200 nm line arrays at 294 K, and synthetic TDTR data (b) at 1 MHz fitted with traditional Fourier model. Best fit with four-parameter model for the same experimental data (c) and synthetic data (d), respectively. The discrepancy in phase that occurs when fitting experimental data with the traditional Fourier model is qualitatively reproduced when fitting the synthetic data. The four-parameter model fits both the experimental and synthetic data well.

2. Interface conductance

Figures S2a and S2b show the interface conductance versus heating frequency and spatial period L, respectively, at various temperatures. The interface conductance increases as the heating frequency increases; there is no clear trend for the interface conductance on the period of the pattern, confirming the assumption that interface conductance primarily depends on heating frequency rather than spatial frequency. We further support the observed trends by applying the four-parameter model to synthetic TDTR data. As shown in Fig. S2b, the measured trends are in good qualitative agreement with these calculations.

3. Modulation frequency dependence of thermal conductivities

Figure S3 shows the thermal conductivities versus modulation frequency from 0.5 MHz to 15 MHz at room temperature and 150 K for w = 117 nm and L = 200 nm line arrays. Little dependence on modulation frequency is observed, confirming our assumption that the thermal conductivity primarily depends on spatial frequency rather than temporal frequency.

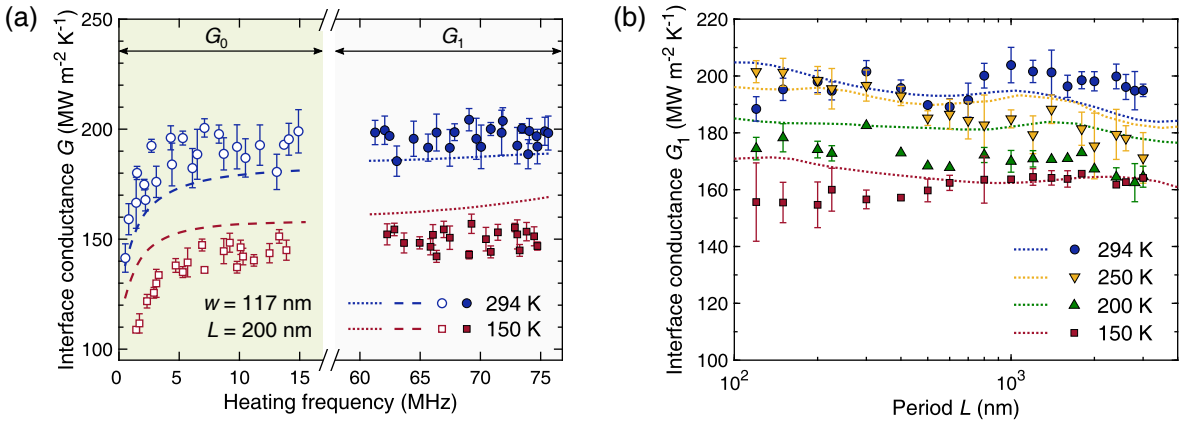

FIG. S2: Interface conductance of nanoline array. (a) Interface conductance versus heating frequency at different temperatures from measurements (symbols) and synthetic TDTR data (lines). Here, G_0 is the interface conductance at heating frequencies less than 10 MHz while G_1 is represented as the interface conductance above 65 MHz, corresponding to the first harmonic. (b) Interface conductance G_1 versus period from measurements (symbols) and synthetic TDTR data (dotted lines). The interface conductance primarily depends on heating frequency. Note that the interface conductance from the synthetic data has been scaled to be comparable to the magnitude of experimental values to facilitate comparison.

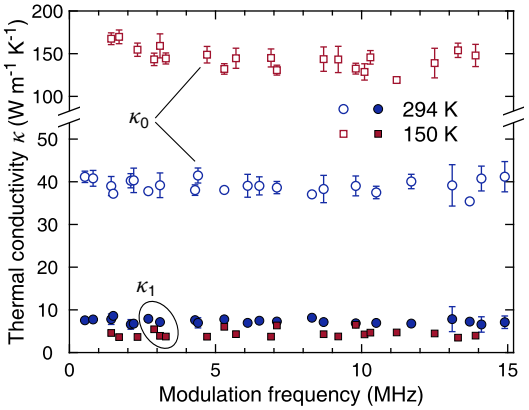

FIG. S3: Thermal conductivity versus modulation frequency. Thermal conductivity κ_0 (open symbols) and κ_1 (filled symbols) versus modulation frequency at 294 K (blue circles) and 150 K (red squares). The thermal conductivity weakly depends on the modulation frequency. The error bar indicates the standard deviation from multiple measurements at each modulation frequency and the uncertainty from fitting (see following Sections 4 and 5).

4. Sensitivity and uncertainty analysis

Here, we present an analysis of how the TDTR signal is affected by the four free parameters in our model. The traditional definition of sensitivity is to examine the fractional change in the signal as a parameter is varied, holding others constant [45, 33]. For the present model, this definition is problematic because different parameters can affect the decay signal in a way that cannot necessarily be compensated by other parameters. Therefore, the sensitivity values computed using the traditional definition may not accurately reflect the overall sensitivity of a parameter to the final predicted decay curve.

We first confirm the necessity of the four-parameter model. Figure S4 shows the best fit with a 3-parameter model (κ, G_0, G_1) obtained by forcing $\kappa_0 = \kappa_1$. The best fit curve lies outside the uncertainty of the experimental data. As κ_1 is a key parameter in our analysis, we also compute the change in signal when κ_1 is varied, all other parameters being held constant. Figure S4 shows the errors from the model calculation with κ_1 at $\pm 20\%$ of the best fitted value and other parameters fixed are larger than the uncertainty in the raw TDTR data, indicating a sufficient sensitivity of κ_1.

We next discuss the uniqueness of the fitting. Qualitatively, we find that a reasonably close initial guess for κ_1 will yield a unique set of 4 parameters for each experimental data set, while an initial guess that is far from this parameter set will fail to converge. For additional checks, we fix one of the 4 parameters at the value of $\pm 15\%$ off the best fitted value, and let the other 3 as free parameters to be varied for the best fit to the data. A representative set of fitting errors is shown in Fig. S5, in which the

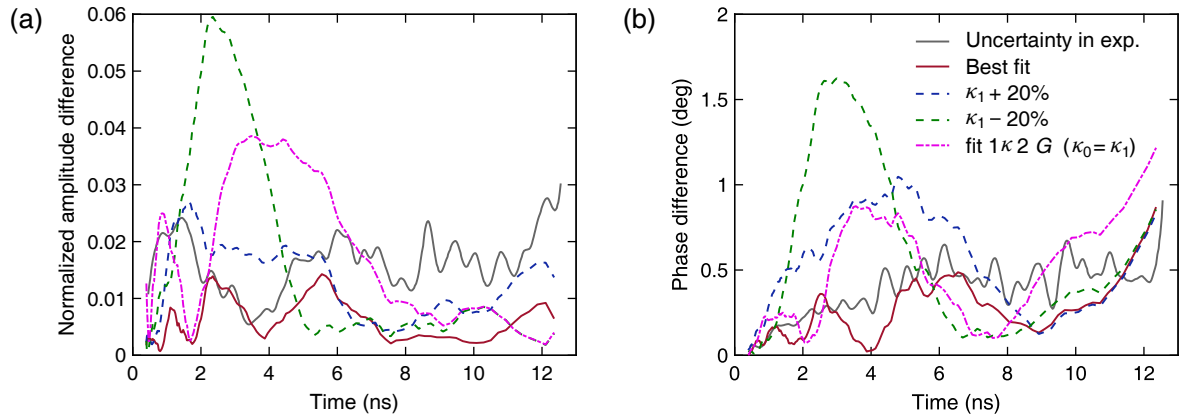

FIG. S4: Fitting errors for experimental data. Uncertainty in the raw TDTR data (solid grey lines) and representative errors of TDTR data in (a) amplitude and (b) phase from best fitting with four-parameter model (solid red line), and 20% bounds of on the fitted κ_1 in the model (dashed blue and green lines), and the fitting with κ_0 = κ_1 and all parameters free (dash-dot magenta lines). The TDTR data is the same as shown in Figs. 1f and 2c in main text with w = 117 nm, L = 200 nm, at 3.1 MHz, 150 K. The dashed blue and green lines show the errors from the model calculation with the κ_1 at $\pm$20% off the best fitted value and other parameters fixed are segmentally larger than the uncertainty in the raw TDTR data. The same situation happens on the errors from the 3-free parameter (κ, G_0, G_1) fittings.

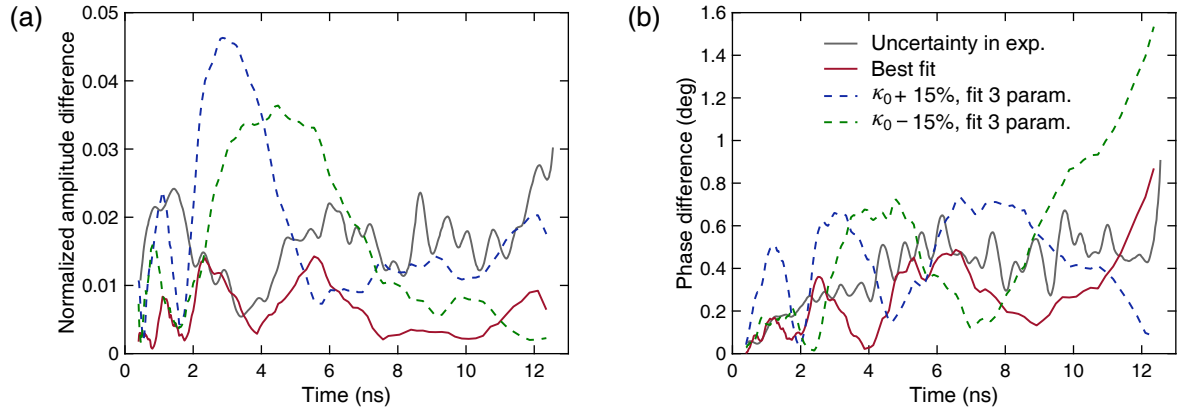

FIG. S5: Fitting errors from different fitting procedures for experimental data. Uncertainty in the raw TDTR data (solid grey lines) and representative fitting errors of TDTR data in (a) amplitude and (b) phase from best fitting with four-parameter model (solid red line), and the fitting with κ_0 fixed at $\pm$15% off best fitted value and other 3 parameters free (dashed blue and green lines). The dashed lines show the errors from 3-parameter fittings are distinctly larger than the best fit in the amplitude and exceed the uncertainty of the data, which means the 15% variation of best fitted value for κ_0 cannot be compensated by the other 3 parameters.

κ_0 is fixed at $\pm 15\%$ off the best fitted value, and the other 3 parameters are free. The errors from the 3-free parameter fittings with κ_0 fixed are distinctly larger than those from the four-parameter model and are also larger than the uncertainty in the raw TDTR data, which means the change of one of the four parameters cannot be compensated by others, supporting the uniqueness of the four-parameter fitting. The uncertainty in the raw TDTR data is determined by calculating the standard deviation of both normalized amplitude and phase data for multiple runs and multiple locations on a sample.

To estimate how uncertainty of one parameter affects the others, we change one parameter (G_0, G_1, κ_0, κ_1) by 10%, then use κ_0 or κ_1 as the only free parameter to fit while keeping all other parameters constant. An example is shown in Fig. S6, in which κ_0 is changed by 10% and κ_1 is the only free parameter (other cases, like changing G_0 and fitting κ_1 give much worse fitting quality and are not shown here). Clearly the errors are much larger than the best fitting with the four-parameter model and are also larger than the uncertainty in the raw TDTR data. Therefore, we estimate uncertainty by making the largest possible change to the chosen parameter that still can still be corrected by variations in other parameters to within the uncertainty of the data. The fitted data are listed in the following Table S1, which shows the new best fit for κ_1 when κ_0 changes by 10% and 5%.

Uncertainties in the fitting parameters also arise due to uncertainties in physical dimensions such as linewidth. We estimate how the uncertainty in the linewidth, w, affects the uncertainty in the free parameters in the following manner. First, we vary w by an amount, hold 3 parameters fixed, and vary one parameter. As κ_1 is the most important parameter for this work, we

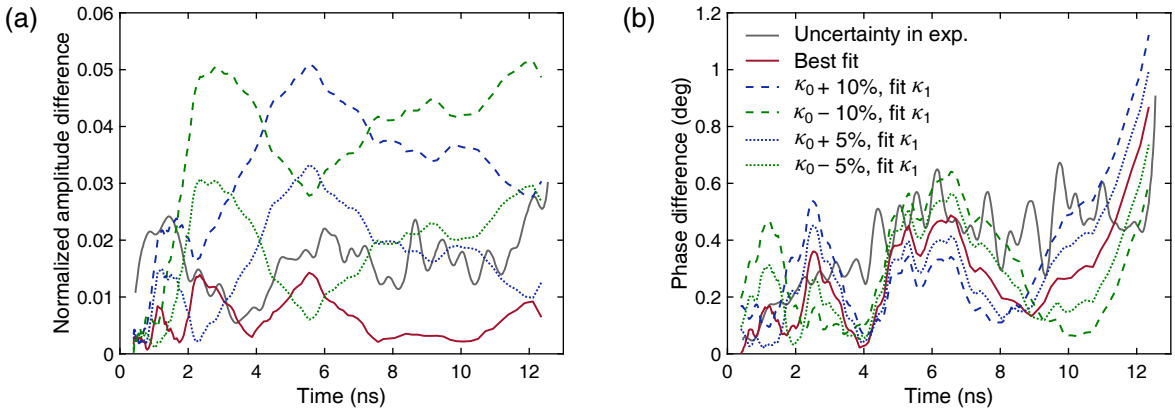

FIG. S6: Estimates of the uncertainty of one parameter due to uncertainties in another. Representative fitting errors of TDTR data in (a) amplitude and (b) phase from best fitting with four-parameter model (solid red line), and the fitting with κ_0 fixed at $\pm$10% or $\pm$5% off best fitted value and only κ_1 free (dashed green and black lines). The TDTR data is the same as shown in Figs. 1f, 2c, S4, and S5. The corresponding values of κ_1 for changes in κ_0 are shown in Table S1.

Table S1: The best fitting of four-parameter model and fitting with only 1 free parameter as described in Fig. S6, w = 117 nm, L = 200 nm, at 3.1 MHz, 150 K.

Different fitting procedures				
	κ_0 (W m^{-1} K^{-1})	κ_1 (W m^{-1} K^{-1})	G_0 (MW m^{-2} K^{-1})	G_1 (MW m^{-2} K^{-1})
four-parameter fit	141.6	3.6	137	155
Fit κ_1 only	141.6 × 0.9	3.5		
	141.6 × 0.95	3.6		
	141.6 × 1.05	3.7		
	141.6 × 1.1	3.8		

show the analysis when κ_1 is varied. Figure S7 shows the quality of fitting is rather poor with κ_1 free and other 3 parameters fixed when w is changed by 10%. Instead, variations in all the fitting parameters may be required to compensate uncertainties in other parameters.

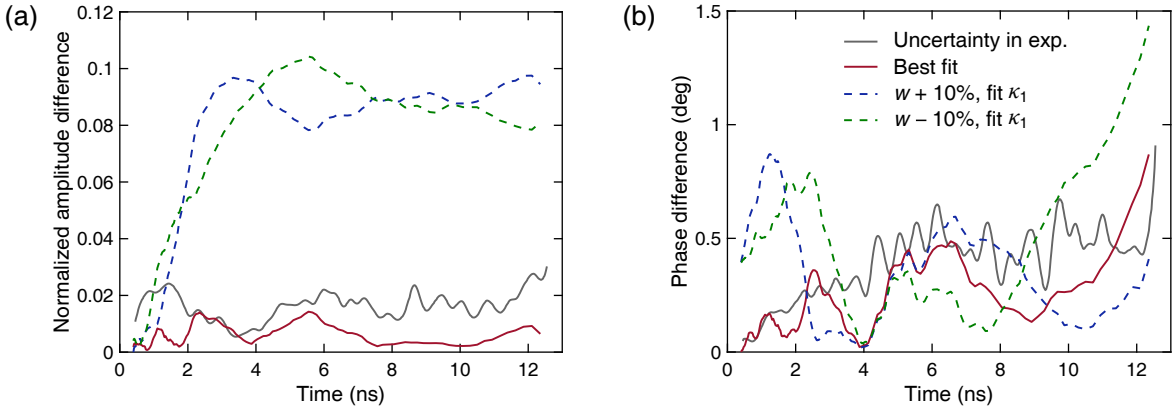

FIG. S7: Procedure to check the compensation of a non-fitting parameter by a fitting parameter. Representative fitting errors of TDTR data in (a) amplitude and (b) phase from best fitting with four-parameter model (solid red line), and the fitting with w fixed at $\pm$10% off measured value and only κ_1 free (dashed green and black lines). The TDTR data is the same as shown in Figs. 1f, 2c, S4, S5, and S6. The dashed lines show the errors are far larger than the best fit in the amplitude and exceed the uncertainty of the data, which means a 10% variation of w cannot be compensated by κ_1 only.

Therefore, to estimate uncertainty from parameters like linewidth, we allow all fitting parameters to vary when w is altered. The uncertainty is estimated from the changes in all fitting parameters from the change in the altered parameter. Figure S8 shows how the fitted thermal conductivity from both the traditional fitting model and four-parameter model change with 10 nm variation in the linewidth. With the traditional fitting procedure, for linewidths above 500 nm (periods larger than 1 μm), the 10 nm change in linewidth does not make an observable difference in the fitting. However, for linewidths less than 500 nm, an error of 10 nm in linewidth is sufficient to reshape the trends of the fitted thermal conductivity versus period. For instance, overestimating or underestimating the linewidth by 10 nm causes a 40% and 20% change in thermal conductivity for line arrays with period of 120 nm and 200 nm respectively. With the four-parameter model, the trend of κ_1 is not noticeably affected. κ_0 is affected in a similar way as the thermal conductivity fitted by the traditional model: as the linewidth decreases, the sensitivity of κ_1 increases gradually. For the smallest pattern in the experiments (w = 55 nm, L = 120 nm), it varies by as much as 48% and 25% with w $\pm$10 nm, respectively. Therefore, it is essential to determine the linewidth accurately to within a few nanometers.

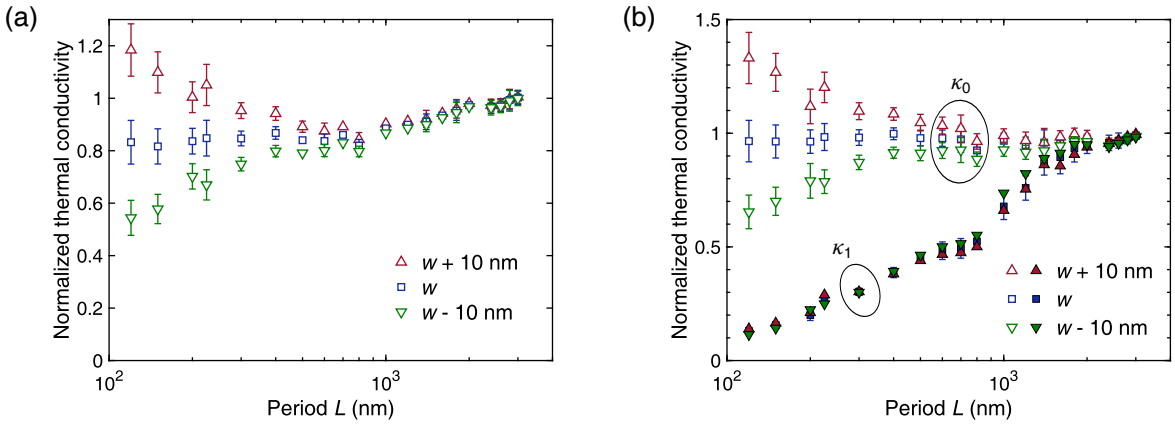

FIG. S8: Fitting results with 10 nm variation in linewidth. Fitted thermal conductivity with $w \pm 10$ nm for both (a) traditional fitting model and (b) four-parameter fitting model. κ_0 is sensitive the linewidth especially for line arrays with smaller linewidth or period. κ_1 is not sensitive to the 10 nm variation in linewidth.

5. Determining linewidth of the patterns

We used atomic force microscopy (AFM) to characterize the dimensions of the lines. Due to the tip convolution artifacts and inaccurate maps for steep edges in AFM measurements, the accuracy for smaller lines on the order of 100 nm is degraded. Consequently, cross-sectional transmission electron microscopy (TEM) images are used to characterize several samples with linewidth less than 150 nm. Representative TEM images and AFM topography for the same line array are shown in the Fig. S9. The ideal shape of the cross-section of a line is a rectangle, which is also used in the diffusive fitting model, while the actual shape is close to trapezoid as shown in TEM cross-section images in Fig. 1d in main text and Fig. S9a owing to fabrication limitations. We approximate the trapezoid-like cross-section as a rectangle by considering the following aspects. First, the interface conductances strongly depend on the contact area between the transducer lines and the substrate, or the bottom base of the trapezoid-like shape. Second, the TDTR signal is extremely sensitive to the thermal capacitance of the lines which depends on its volume (the cross-sectional area of the lines shown in 2D images). After decoupling into κ_0 and κ_1, only κ_0 is sensitive to the cross-section area. Furthermore, κ_1 is not sensitive to either the cross-sectional area or the linewidth. Consequently, the linewidth is chosen as the bottom base of the trapezoid-like shape, while the thickness of the lines is determined by the cross-sectional area divided by the linewidth.

For AFM measurements, we obtained the linewidths using an average over around 3-5 lines and with a correction for the tip radius and sidewall reconstruction. The typical difference in size obtained from AFM and TEM was less than 3 nm. We considered the uncertainty of linewidth with $w \pm 3$ nm (with $w < 150$ nm), and $w \pm 5$ nm in the fitting to account the uncertainty in the fitted results for others.

6. Reproducibility on different samples

The experimental results from two different samples are shown in Fig. S10. The thermal conductivity κ_0 and κ_1 of the two samples are almost overlapped for all periods. Although the interface conductance depends on the fabrication processing, the

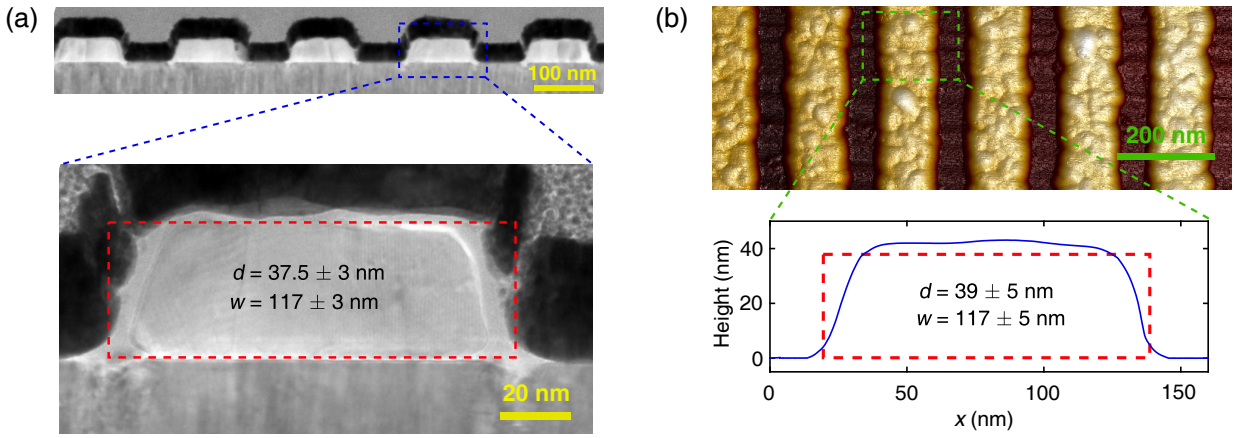

FIG. S9: Linewidth determination from TEM cross- section image and AFM topography. (a) Representative TEM cross-section of 100 nm (designed value for linewidth) lines with period of 200 nm. The linewidth is 117 $\pm$ 3 nm measured at the bottom of the trapezoid-like cross-section of one line. The effective thickness of the line is calculated to be 37.5 $\pm$ 3 nm. The standard deviations come from measurements on more than 5 lines. (b) AFM topography for the same line array as (a). The cross-section profile shown at the bottom is an average over the area indicated in green in the AFM topography at top. Tip convolution artifacts have been removed in the cross-section profile. Further, both sides of the line have been reconstructed by considering the slope measured from TEM as presented in (a), which is $\sim$70°. The measurement is consistent with the AFM determined linewidth which is averaged over 3 areas in AFM topography, with slightly higher standard deviation than in TEM.

maximum variation of averaged G_1 in Fig. S10b is 10%, indicating our fabrication process is reproducible.

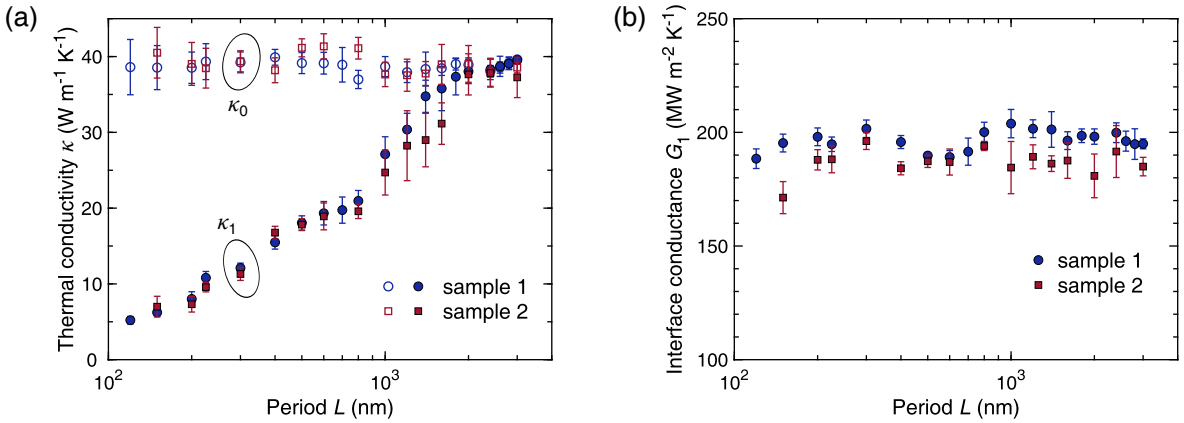

FIG. S10: Thermal conductivity and interface conductance measured from different samples. (a) Thermal conductivity κ_0 (filled symbols) and κ_1 (open symbols) of sample 1 (blue cycles) and sample 2 (red squares). Sample 1 data has been presented in the main text. (b) Interface conductance κ_1 of 2 samples. (a) κ_0 and κ_1 from two samples give close results, showing the repeatability of the experiments. The slight difference in G_1 is caused by variation in fabrication processing.

7. Effect of thermoreflectance of sapphire substrate

In the thermal model with the line array, the sapphire is assumed to be transparent to the 785 nm laser used in the experiment, and the thermoreflectance signal is only from the aluminum lines, and not from the sapphire substrate. In Ref. [16], this assumption was tested by performing two measurements on sapphire: one with the filled gaps by low thermoreflectance metal, and one without; the case without corresponds to our samples. Hu *et al*. reported that measurements with and without the fillers coincided nearly exactly, indicating that the thermoreflectance signal from the sapphire in the gap also has negligible effect the measurements.

We perform an additional check by simply placing the sapphire without a pattern in the TDTR experiment and measuring the signal. Figure S11 shows the intensity of raw thermoreflectance signals from sapphire with aluminum line array pattern and

from the sapphire substrate, respectively. The thermoreflectance signal from the sapphire substrate is on the noise level of the detecting system, providing evidence that the thermoreflectance signal from the sapphire is not detectable.

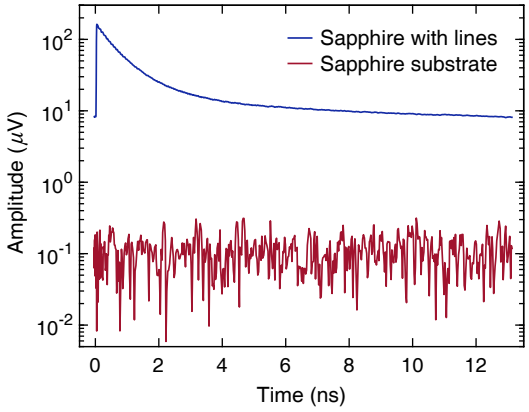

FIG. S11: Thermal reflectance signal for sapphire with line array pattern and without pattern. The thermoreflectance signal intensity from line array on sapphire decays from above 100 μV at the beginning to few μV at the end of the delay. The thermoreflectance signal from sapphire substrate is at the noise level of the detecting system.

References (with the numbers consistent with those in the main text)

[45] B. C. Gundrum, D. G. Cahill, and R. S. Averback, Thermal conductance of metal-metal interfaces, Phys. Rev. B **72**, 245426 (2005).

[33] A. J. Schmidt, X. Chen, and G. Chen, Pulse accumulation, radial heat conduction, and anisotropic thermal conductivity in pump-probe transient thermoreflectance, Rev. Sci. Instrum. **79**, 114902 (2008).

[16] Y. Hu, L. Zeng, A. J. Minnich, M. S. Dresselhaus, and G. Chen, Spectral mapping of thermal conductivity through nanoscale ballistic transport, Nat. Nanotechnol. **10**, 701 (2015).